Rational design of walnut–like ZnO/Co3O4 porous nanospheres with substantially enhanced lithium storage performance

Journal:	*Nanoscale*
Manuscript ID	NR-ART-11-2021-007890
Article Type:	Paper
Date Submitted by the Author:	30-Nov-2021
Complete List of Authors:	Zhang, Yifan; Georgia Institute of Technology, Chemistry and Biochemistry Zhang, Yamin; Georgia Institute of Technology Aldama, Edgar; Georgia Institute of Technology Liu, Huitian; Georgia Institute of Technology, Sun, Zhijian; Georgia Institute of Technology Ma, Yao; Georgia Institute of Technology Liu, Nian; Georgia Institute of Technology, Chemical and Biomolecular Engineering Zhang, Z. John; Georgia Institute of Technology, Chemistry & Biochemistry

SCHOLARONE™
Manuscripts

Rational design of walnut-like ZnO/Co$_3$O$_4$ porous nanospheres with substantially enhanced lithium storage performance

Yifan Zhang[a], Yamin Zhang[b], Edgar Aldama[a], Huitian Liu[b], Zhijian Sun[c], Yao Ma[b], Nian Liu[b]*, Z. John Zhang[a]*

[a]School of Chemistry and Biochemistry, Georgia Tech, Atlanta, GA 30332, USA

[b]School of Chemical and Biomolecular Engineering, Georgia Tech, Atlanta, GA 30332, USA

[c]School of Materials Science and Engineering, Georgia Institute of Technology, Atlanta, Georgia 30332, United States

*Corresponding authors:

nian.liu@chbe.gatech.edu

john.zhang@chemistry.gatech.edu

Abstract

Rational fabrication and smart design of multi-component anode materials to achieve desirable reversible capacities and exceptional cyclability are significant for lithium-ion batteries (LIBs). Herein, walnut-like ZnO/Co_3O_4 porous nanospheres were prepared by a facile solvothermal method, which were then applied as a mechanically stable anode material for LIBs. The rationally designed hybridized electrode brings favorable structural features, particularly ZnO/Co_3O_4 porous nanospheres with abundant vacant space and enhanced surface area, enhancing lithium/electron transport and relieving volumetric stresses during the cycling process. Moreover, several in-situ hybridized anode materials with electrochemical cooperation further overcome the challenge of capacity decay and conductivity deficiency. The as-obtained ZnO/Co_3O_4 delivered a much better lithium storage performance compared with ZnO, Co_3O_4, and their physical mix. We believe that the novel design criteria will bring opportunities in exploration and promote the practical application of transitional metal oxides.

1. Introduction

Up to date, lithium-ion batteries (LIBs) are one of the major energy sources.[1–3] With the rapid development of modern devices such as large-scale energy storage devices and electric vehicles, further improvement in energy/power densities, safety and lifespan are required for LIB.[4] Graphitic materials are the main commercial anodes because of their chemical stability, low operating voltage versus Li/Li^+ and low cost, but are still limited by their poor theoretical specific capacities (LiC_6, 372 mAh g^{-1}).[5] Therefore, it is significant to explore advanced anode materials for LIBs.

Transition metal oxides (TMOs) hold substantial promise for LIBs since they can reversibly accommodate Li^+ through conversion or alloying reactions, which involve the formation and decomposition of lithium oxide.[6–8] Creating chemical bonds through chemical reactions between Li^+ and active materials is conducive to high-performance anode materials, in which multi-electron transfer occurs and superior reversible capacity can be expected.[6] However, their practical application in LIBs is limited by a short cycling life due to several intrinsic reasons: severe volume variation during lithiation/delithiation, pulverization of electrode active materials and slow ionic/electronic conductivity.[6,9–11] Therefore, it is of great significance to surpass the above-mentioned issues and boost their electrochemical performance. For TMOs, nanostructure engineering and hybridization of different phases can be efficacious strategies.[12–15]

Regarding nanostructure engineering, fabricating porous particles at the nano/microscopic level can effectively recover the lithium storage performance.[16–23] For example, Wang et al.

successfully prepared porous $CoMoO_4$ nanorods that exhibited a capacity of 603 mAh g^{-1} at 400

mA g^{-1}.[24] Due to their extra void space and large surface area, these specially designed structures

counteract structural strains upon cycling, enlarge electrode/electrolyte interface to offer more

reactive sites, and promote Li^+ diffusion. Besides nanostructure engineering, hybridization of

several active materials has been reported as another promising strategy, since the heterojunctions

are beneficial for electron/ion diffusion, mechanical stability and redox reaction kinetics.[6,25] Both

charge carrier transport and interfacial reaction kinetics can be enhanced by building

heterostructures composed of several coupling components with different bandgaps.[26] In this

regard, Fe_2O_3/MnO_2[27] and $Co_3O_4/CoMoO_4$[28] have been reported to show extraordinary lithium

storage performance. Taken together, achieving synchronous combination of structural

engineering at the nano/microscopic level and hybridization of TMOs will be an effective path

towards LIBs with high lithium storage performance.

Among various TMO candidates, ZnO has a relatively high capacity (978 mAh g^{-1}) because

Zn forms alloy material with Li, indicating a larger amount of Li ions captured.[6,9] It has been

reported by Tarascon et al. that the "over capacity" was associated to the growth of SEI films and

TEM was conducted to deduce this. In addition, they confirmed the catalytic role of Co in the

generation of SEI films.[29] Therefore, it is promising to fabricate Co_3O_4-containing ZnO hybrid

materials. However, fabricating in-situ hybridized nanomaterials through one-pot synthesis while

keeping an advantageous architecture is hard to achieve.
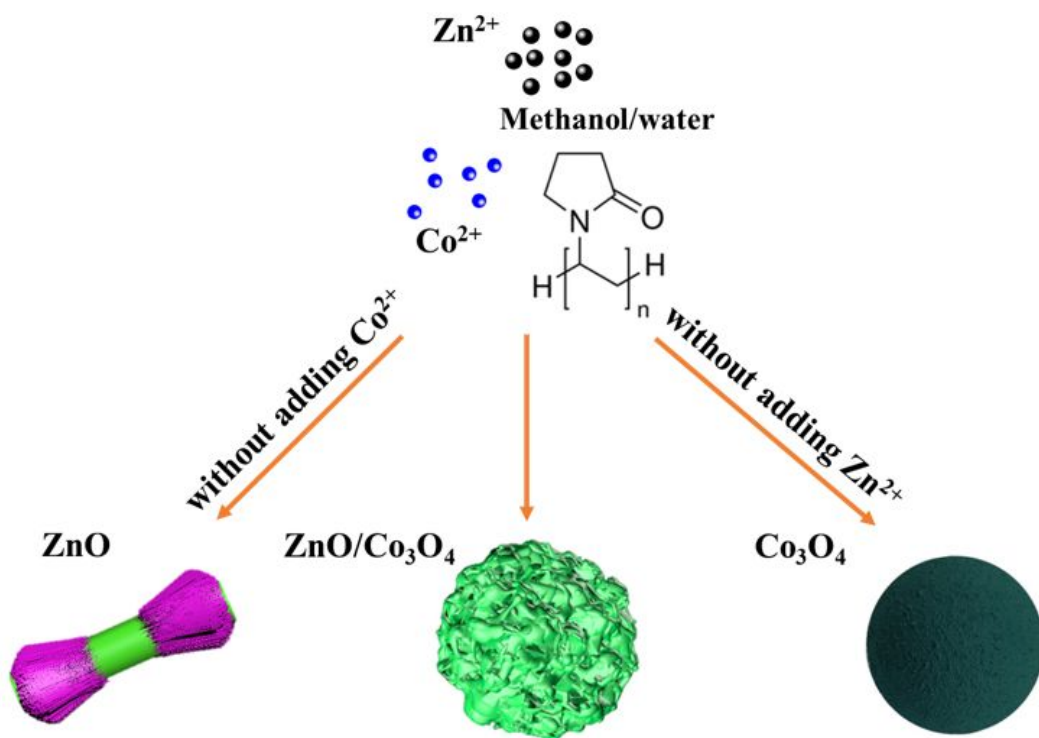
Fig. 1 Diagram for the fabrication of ZnO, Co_3O_4 and ZnO/Co_3O_4.

Herein, walnut-like ZnO/Co_3O_4 porous nanospheres were synthesized for the first time by a solvothermal route, possessing great structural advantages (**Fig. 1**). Specifically, the structure of porous nanospheres with ravines could benefit the transport of lithium ions, provide abundant electrochemically active sites, and offer structural flexibility as it prevents the electrode from collision or deformation arising from huge volumetric change. Moreover, the in-situ hybridization of ZnO and Co_3O_4 brings a synergistic effect, which endows the electrode with improved electronic conductivity and reinforced structural stability. The as-prepared ZnO/Co_3O_4 porous nanospheres exhibited enhanced electrochemical activity, superior cycling stability and high

specific capability. The reported one-pot colloidal synthesis route is promising and can be extended to design other multi-component hierarchical TMO nanostructures.

2. Materials and methods

2.1. Synthesis

1.2 g $Zn(NO_3)_2 \cdot 6H_2O$ (Alfa Aesar), 0.8 g $Co(NO_3)_2 \cdot 6H_2O$ (J.T. Baker) and 1 g PVP (Alfa Aesar) were dissolved and stirred in methanol/DI water (86/10 mL) solution for 40 min, which was then heated in an autoclave at 180 °C for 6 h. The resulting precipitates were collected and washed with DI water five times, followed by drying and annealing in air at 450 °C for 40 min.

For comparison, ZnO and Co_3O_4 were prepared using 2.0 g $Zn(NO_3)_2 \cdot 6H_2O$ or 2.0 g $Co(NO_3)_2 \cdot 6H_2O$. In addition, physically mixed ZnO/Co_3O_4-PM (weight ratio = 3:2) was prepared by mixing as-obtained ZnO and Co_3O_4.

2.2 Characterization

The morphologies and structural aspects were obtained by transmission electron microscopy (TEM, Hitachi HT7700), high-resolution transmission electron microscopy (HRTEM, Hitachi HD2700), and scanning electron microscopy (SEM, Hitachi SU8230). The crystal structures were determined by Bruker D8 Advanced Powder XRD. X-ray photoelectron spectroscopy (XPS) was achieved with the Thermo K-Alpha XPS system. The pore features and Brunauer-Emmett-Teller surface area were characterized by physisorption (Microtrac BEL Corporation).

2.3. Electrochemical measurements

Active materials, super P carbon black (MTI Corporation) and sodium carboxymethyl

cellulose (M_w 250000, Sigma Aldrich) were mixed with a weight ratio of 8:1:1 in DI water. The slurry was then cast on copper foil, followed by dehydration at 120 °C overnight. Cells were assembled utilizing Li metal as the counter electrode, 1M $LiPF_6$ in EC/EDC (v/v = 1:1, Sigma Aldrich) as the electrolyte, and Celgard 2400 as the separator. Cyclic voltammetry (CV) was performed between 3.0 and 0.01 V at 0.2 mV s^{-1}. Electrochemical impedance spectroscopy (EIS) measurements were measured between 100 kHz and 0.01 Hz.

3. Results and discussion

The synthetic procedure of walnut-like ZnO/Co_3O_4 involved two steps, a solvothermal method using PVP as the surfactant, followed by an annealing process at 450 °C in the air for 40 min. **Fig. S1** shows the SEM images of ZnO/Co_3O_4 samples obtained under different reaction time (1, 2 and 3 h), respectively. The formation of walnut-like ZnO/Co_3O_4 nanospheres goes through three stages: (1) the generation of spherical particles by the solvothermal reactions between metal nitrates and PVP; (2) the capping of PVP: sufficient PVP forms a continuous layer to warp the whole surface of nanospheres and promotes the growth in all direction. As the reaction progresses, relatively excessive metal nitrates and insufficient dosages of PVP are not able to form a continuous outer layer of the nuclei, resulting in the growth of exterior nanorods in the lateral directions and the walnut-like surface is generated; (3) the growth of walnut-like nanospheres via Ostwald Ripening and finally reach the best stabilization status. The annealing temperature was determined through TGA analysis (**Fig. S2**). Here, 450 °C was chosen as the annealing temperature to ensure a

complete decomposition of precursors. A mass loss (~5.6%) can be observed below 400 °C, which can be assigned to the decomposition of organic content and evaporation of the absorbed solvent.[30] The formation of ravines was observed after annealing, resulting in a walnut-like morphology. Besides, the surface became rugged and porous, arising from the elimination of organics during the annealing process.[6] When the annealing temperature further increases to 550 and 650 °C, the collapse of 3D structure and formation of debris could be observed (**Fig. S3**). Thus, the annealing temperature was set at 450 °C. It is interesting to find that ZnO and Co_3O_4 displayed significantly different morphologies: dumbbell-like ZnO and sphere-like Co_3O_4, both featuring a relatively smooth surface, suggesting that both Zn^{2+} and Co^{2+} are significant to generate walnut-like ZnO/Co_3O_4 (**Fig. 1**).

In **Fig. S4**, 0.4 g of ZnO/Co_3O_4 and graphite were shown. Compared with commercial graphite, ZnO/Co_3O_4 occupied less volume with a larger packing density, which is important for LIBs to achieve high volumetric energy density.[6,31] Thus, ZnO/Co_3O_4 is promising to replace graphite when applied as anode for LIBs.
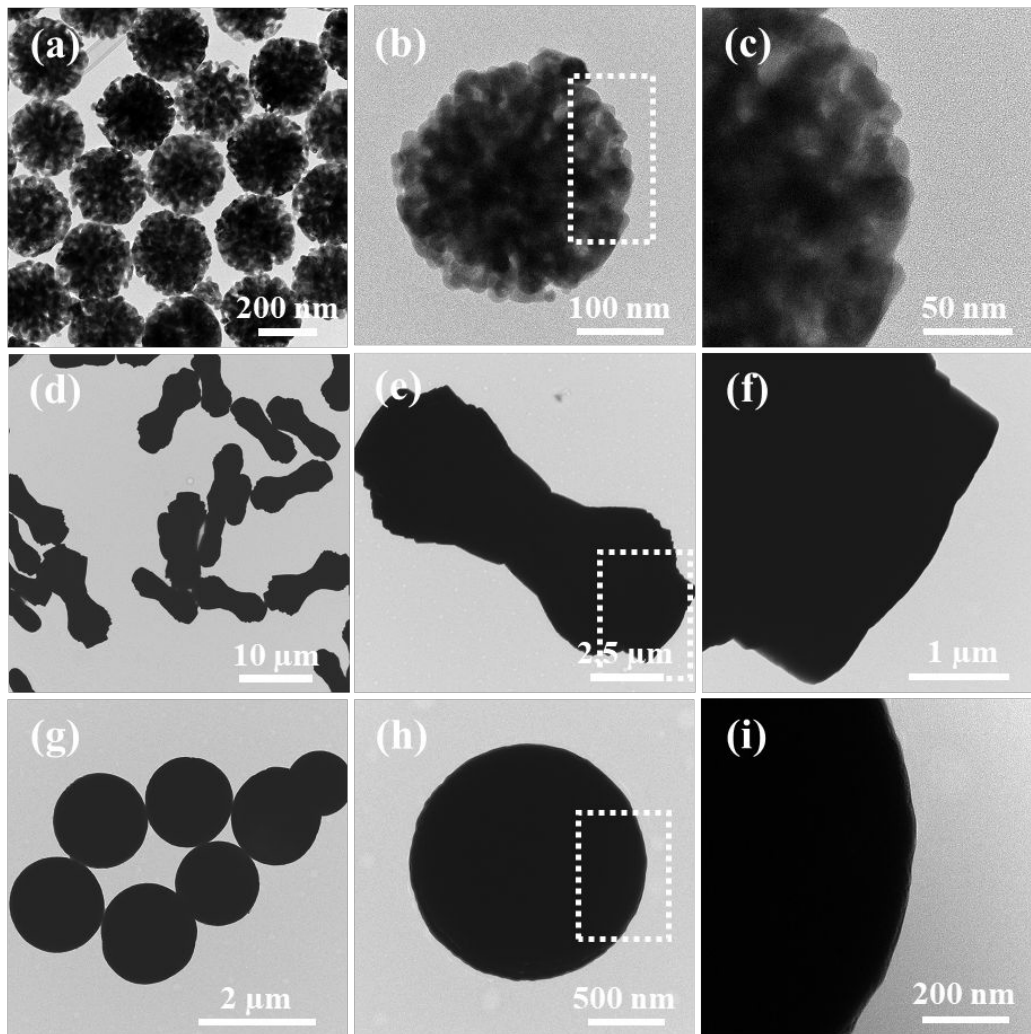
**Fig. 2** TEM images of (a-c) ZnO/Co$_3$O$_4$, (d-f) ZnO and (g-i) Co$_3$O$_4$.
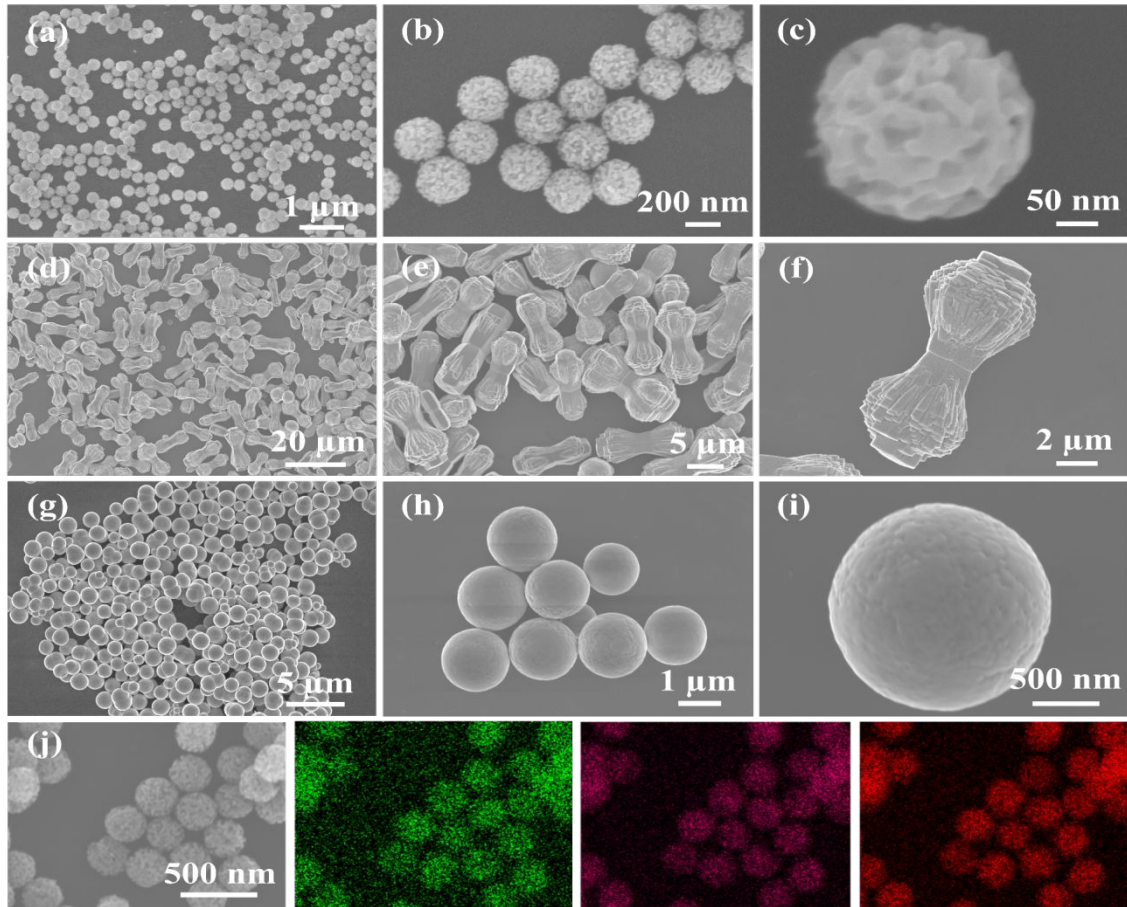
Fig. 3 SEM images of (a-c) ZnO/Co$_3$O$_4$, (d-f) ZnO and (g-i) Co$_3$O$_4$. (j) Spatial distributions of Zn, Co and O in ZnO/Co$_3$O$_4$.

TEM and SEM were performed on ZnO/Co$_3$O$_4$, ZnO, Co$_3$O$_4$ and their corresponding solvothermal precursors. TEM images in **Fig. 2** confirmed the porous feature of ZnO/Co$_3$O$_4$, which could effectively alleviate volume change upon cycling and promote electrolyte penetration. As shown in **Fig. 3**, the panoramic overview demonstrated the successful synthesis of highly uniform and dispersed ZnO/Co$_3$O$_4$ consisting of walnut-like porous nanospheres with a diameter of around 250 nm. Compared with solvothermal precursors (**Fig. S5** and **Fig. S6**), the morphology of

ZnO/Co_3O_4 was well-maintained, but with a relatively rougher surface and deeper ravines. The uniform distribution of Zn and Co elements in our ZnO/Co_3O_4 is important for the battery performance and was confirmed using scanning transmission electron microscopy (STEM) image and elemental mappings (**Fig. S7**). Also, HRTEM image (**Fig. S8**), shows close proximity between small domains of ZnO and Co_3O_4. As a result, a strong E-field was introduced by large energy bandgap difference between ZnO and Co_3O_4 (2.07 eV for ZnO, and 3.2 eV for Co_3O_4), thus electron/ion diffusion and surface redox reaction kinetics were facilitated.[25,32] As shown in **Fig. 2** and **Fig. 3**, ZnO exhibited a dumbbell morphology with a large aspect ratio, while Co_3O_4 exhibited a spherical morphology. Their relatively smooth surfaces limit their lithium storage performances.
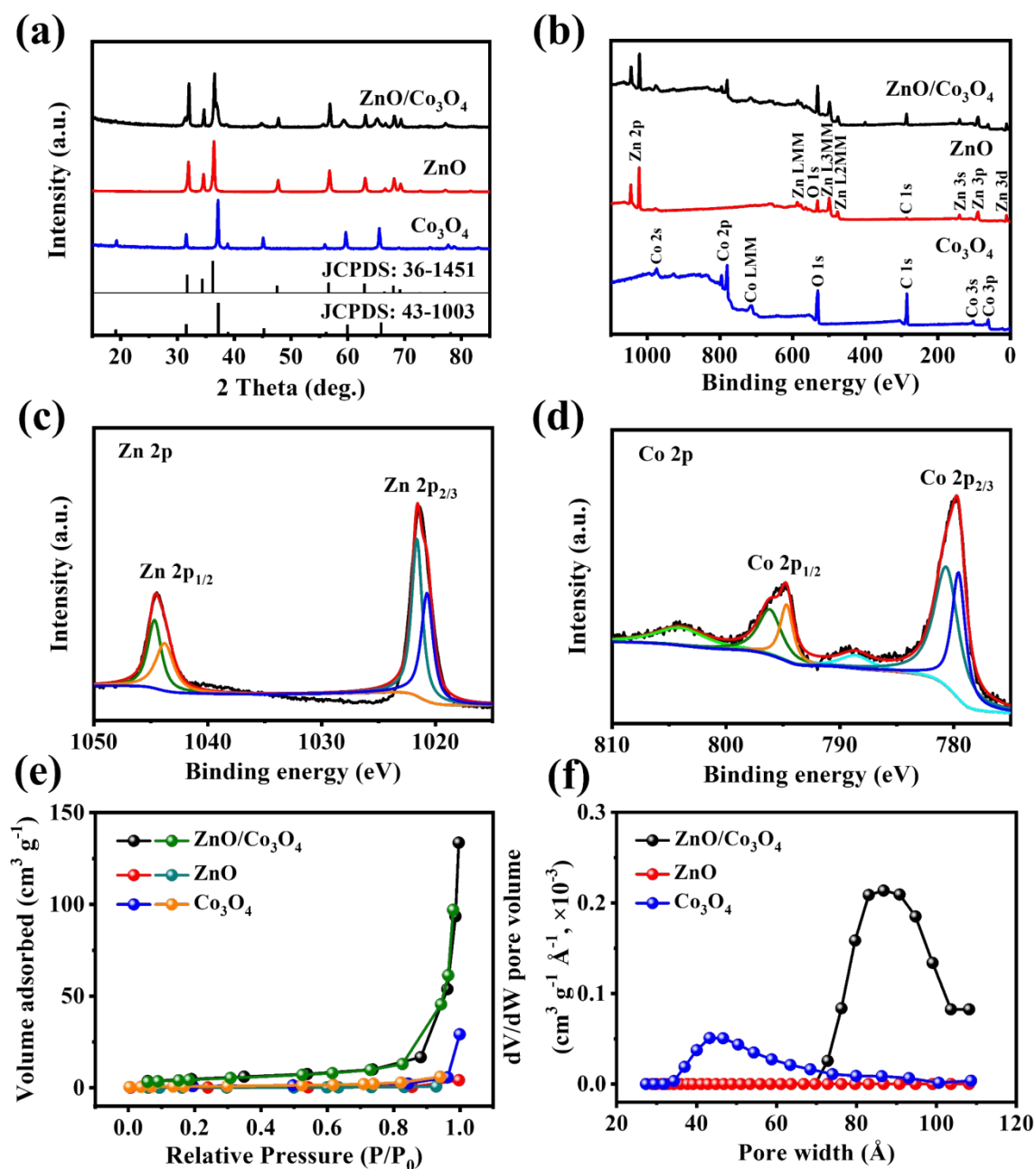
Fig. 4 (a) XRD and (b) XPS spectra of ZnO/Co$_3$O$_4$, ZnO and Co$_3$O$_4$. XPS spectra of elemental components (c) Zn and (d) Co elements in ZnO/Co$_3$O$_4$. (e) BET curves and (f) pore width distribution of ZnO/Co$_3$O$_4$, ZnO and Co$_3$O$_4$.

As shown in **Fig. 4a**, peaks at 31.9°, 34.6°, 36.4°, 47.7°, 56.8° and 63.0° were assigned to (1 0 0), (0 0 2), (1 0 1), (1 0 2), (1 1 0) and (1 0 3) crystal planes of ZnO, and the remaining peaks located at 19.0°, 31.4°, 36.9°, 44.9°, 59.5° and 65.4° corresponded to the (1 1 1), (2 2 0), (3 1 1), (4 0 0), (5 1 1) and (4 4 0) planes of well-crystallized Co_3O_4.[6,33] XPS was performed to determine elemental valence states. As can be seen from **Fig. 4b**, the wide XPS survey spectrum confirmed the existence of Zn, Co and O. Meanwhile, two peaks at 1044.5 and 1021.4 eV in the high-resolution Zn 2p spectrum (**Fig. 4c**) were related with Zn $2p_{1/2}$ and Zn $2p_{3/2}$, implying the existence of Zn^{2+}.[6] Co 2p spectrum (**Fig. 4d**) showed two couples of peaks at 795.1 and 779.9 eV, corresponding to Co $2p_{1/2}$ and Co $2p_{3/2}$, respectively, suggesting the formation of Co_3O_4.[33] These XPS analyses are consistent with the XRD result. Specific surface area and porous structural characteristics influence the lithium storage performance of electrode materials,[34] thus the porous nature of ZnO/Co_3O_4 was investigated by Brunauer-Emmett-Teller analysis (BET). As observed in **Fig. 4e** and **Fig. 4f**, ZnO/Co_3O_4 exhibited a porous feature, and the specific surface area was 17.55 m^2 g^{-1}, much larger compared with ZnO and Co_3O_4 (0.75 and 2.91 m^2 g^{-1}, respectively) (**Table S1**). Large surface area and rich pores bring effective electrode/electrolyte interaction and offer effective pathways for ion/electron diffusion.[25]
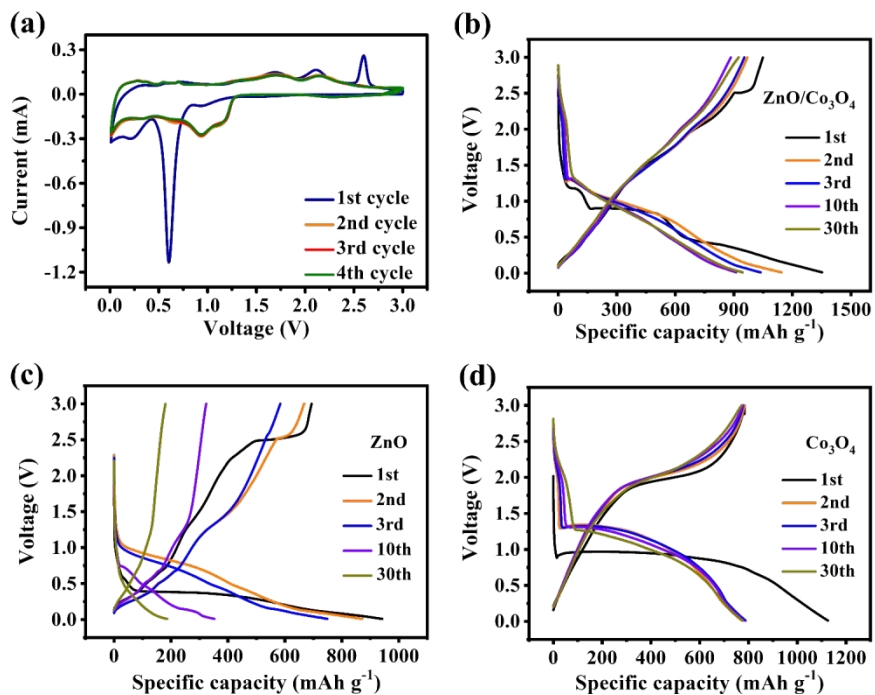
Fig. 5 (a) CV curves of ZnO/Co$_3$O$_4$ at 0.2 mV s^{-1}. Charge/discharge profiles at 0.1 A g^{-1} for (b) ZnO/Co$_3$O$_4$, (c) ZnO and (d) Co$_3$O$_4$.

The electrochemical performance of ZnO, Co$_3$O$_4$ and ZnO/Co$_3$O$_4$ were evaluated. CV curves of ZnO/Co$_3$O$_4$ exhibited a rich redox reaction (**Fig. 5a**). Peaks from 0 to 0.4 V were caused by Li-Zn alloying process.[35,36] The peak at 0.62 V was related to the formation of metallic Co, Li$_2$O and SEI film.[33,35] Meanwhile, the peak at 1.71 V originated from the conversion reaction of Co to Co$_3$O$_4$.[35] Peaks at 2.11 V and 2.61 V corresponded to the reoxidation of Zn.[35] The shift of anode peaks arose from structural reorganization and polarization of electrode materials.[36] Evidently, the overlapped curves demonstrated extraordinary electrochemical reversibility. As indicated by the results of galvanostatic charge/discharge measurement shown in **Fig. 5b**, three obvious plateaus agreed well with CV curves. The well-overlapped discharge/charge profiles indicated good

electrochemical stability. In contrast, as shown in **Fig. 5c** and **Fig. 5d**, both ZnO and Co_3O_4

delivered lower specific capacities compared with that of ZnO/Co_3O_4. Moreover, there was a

severe capacity decay for ZnO, resulting from slow ion/electron transport.[6]
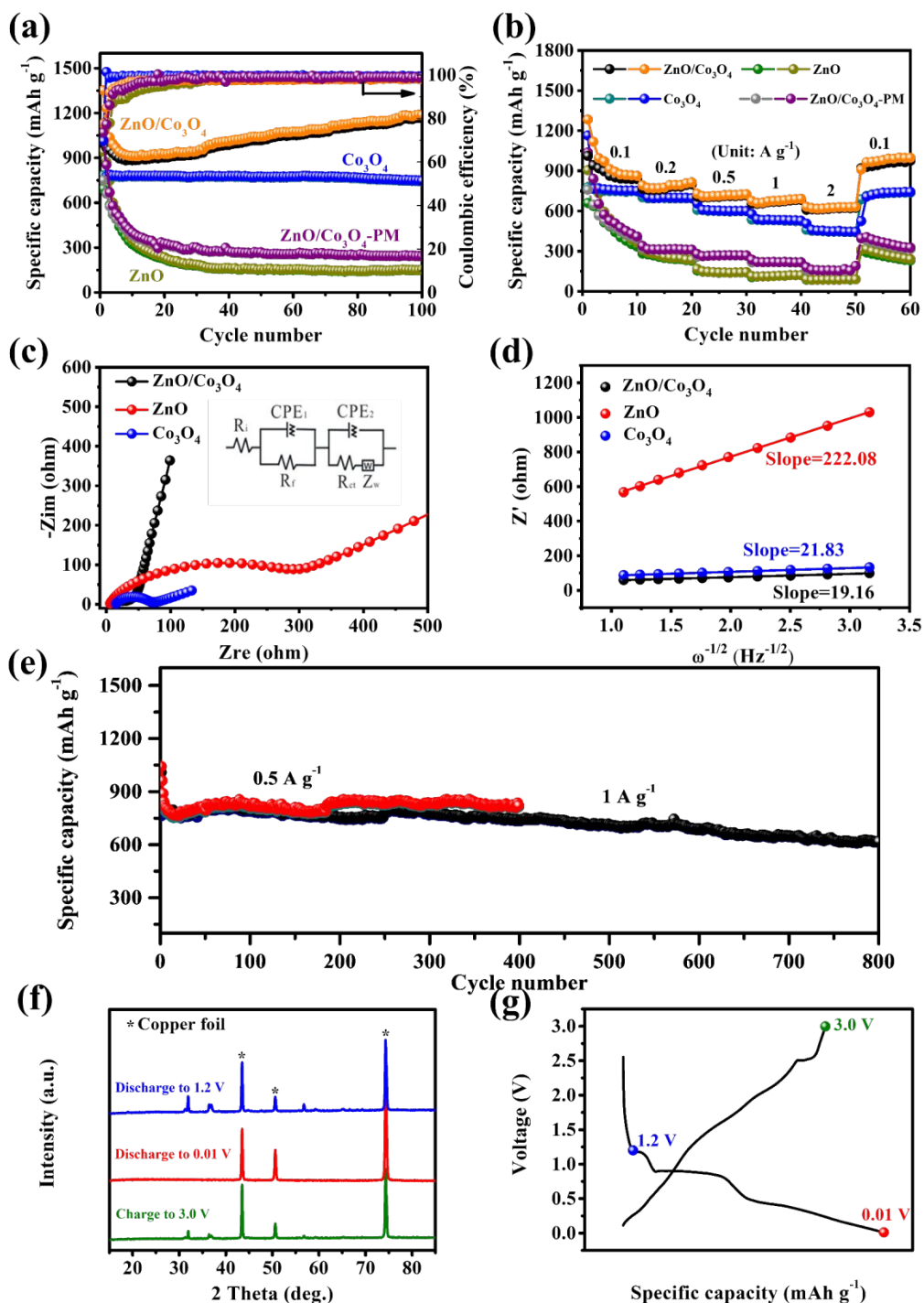
Fig. 6 (a, b) Cycling and rate performance for ZnO, Co_3O_4, ZnO/Co_3O_4, and their physical mix.

(c) Nyquist plots of ZnO/Co_3O_4, ZnO and Co_3O_4 after 100 cycles at 0.1 A g^{-1} and (d) fitted plot

results of Z′ *versus* $\omega^{-1/2}$. (e) Cycling performance of ZnO/Co_3O_4 at large current densities. (f, g)

patterns of XRD analysis of ZnO/Co_3O_4 at different states in initial cycle.

The cycling performances were evaluated at 0.1 A g^{-1}. As shown, discharge/charge capacities

of ZnO/Co_3O_4 in the first cycle were 1352.3/1048.3 mAh g^{-1} (**Fig. 6a**). The capacity decay arose

from the generation of SEI and trapped Li-ions within the electrode.[6] After 10 cycles, the

Coulombic efficiency recovered to over 97%, demonstrating excellent reversibility. The alloying

process of Zn with Li in ZnO/Co_3O_4 might aggravate the issue of low Coulombic efficiency in the

initial cycles. Thus, the volume ratio of ZnO was decreased to see if the low Coulombic efficiency

in first cycles can be solved. As the ratio of ZnO and Co_3O_4 decreased from 3:2 to 1:8, the initial

Coulombic efficiency increased from 80.11% to 94.49%. When controlling the ratio of ZnO and

Co_3O_4, mesoscale pore structure was observed to be adjusted. As shown in **Fig. S11**, the composite

exhibited a smoother surface with a less porous feature when there is more Co_3O_4, which was

further confirmed by BET analysis (**Table S2**). As shown in **Fig. S12**, the cycling performance of

composites with different ratio of ZnO and Co_3O_4 indicates that composites with larger surface

area and richer pores exhibited higher discharge/charge capacities. In addition, it should be noticed

that all ZnO/Co_3O_4 samples exhibited a gradual increase in capacity. This is a common

phenomenon for oxide electrodes, which can be attributed to several reasons: (1) the polymeric

gel-like films generated from electrolyte decomposition participate in lithium storage and provide the extra capacity;[9,37] (2) the activation process improves the diffusion of lithium ions;[13] (3) defects are introduced to electrode materials upon repeated lithiation/delithiation, bringing more active sites and promoting the reaction activity.[6,33,38,39] After 100 cycles, the capacity retained at 1187.4 mAh g^{-1}. Unlike ZnO/Co₃O₄, the ZnO electrode exhibited a sharp capacity attenuation from 941.9 to 151.9 mAh g^{-1}, while the Co₃O₄ electrode delivered a relatively poor capacity of 746.9 mAh g^{-1}. The lithium storage performances of physically mixed ZnO and Co₃O₄ were also investigated. After 100 cycles, the capacity could only retain 244.1 mAh g^{-1}, highlighting the significance of in-situ hybridization of ZnO and Co₃O₄. The presence of heterostructures generated from in-situ hybridization of different components greatly enhanced interfacial reaction kinetics and charge carrier transport. Even at 0.5 A g^{-1} and 1 A g^{-1}, ZnO/Co₃O₄ electrode could still exhibit reversible capacities of 821.5 and 618.2 mAh g^{-1} after 400 and 800 cycles, respectively (**Fig. 6e**). In contrast, the performances of ZnO, Co₃O₄ and ZnO/Co₃O₄-PM were unsatisfactory, arising from low surface area and large charge transfer resistance (**Fig. S15**).

EIS analysis also confirmed the electrolyte/electrode activation process of ZnO/Co₃O₄. As shown in **Fig. 6c** and **Fig. S16a**, there was an appreciable decrease in the interfacial resistance from 57.2 Ω to 53.9 Ω, indicating optimized electrochemical kinetics. The activation was related to several reasons: (1) the unique walnut structure is favorable for electron transport and ion diffusion; (2) the electrochemical reaction promotes electrolyte infiltration, thus reducing the electrode/electrolyte interfacial impedance.[40] ZnO/Co₃O₄ exhibited a smaller diameter of 53.9 Ω,

indicating lower charge transfer resistance, further confirming its structural advantage. As exhibited in **Fig. S17** and **S18**, intact nanospheres without any collapse and shedding could be detected for ZnO/Co_3O_4 after 100 cycles, suggesting extraordinary tolerance of lithiation/delithiation. These advantages contribute to enhanced reaction kinetics and electrochemical performance.

The lithium-ion diffusion coefficient was obtained from the equation below:[41]

$$D_{Li}^+ = R^2T^2/2A^2n^4F^4C^2\sigma^2 \tag{1}$$

In the Nyquist plot, the linear curve is related with Li^+ diffusion.[30,42] σ was obtained to be 19.16 Ω $s^{-1/2}$ from the fitted lines of Z' and $\omega^{-1/2}$ for ZnO/Co_3O_4 electrode after cycling (**Fig. 6d**). The larger D_{Li}^+ of ZnO/Co_3O_4 indicates faster transport of electrons and ions, which was conducive to achieve excellent lithium storage performance.

The reversibility of ZnO/Co_3O_4 was further proved by ex-situ XRD measurements (**Fig. 6f**). The peaks at 43.5°, 50.6° and 74.3° originated from Cu.[43] When the ZnO/Co_3O_4 was discharged to 1.2 V, peaks of ZnO and Co_3O_4 could be observed. No peaks related to ZnO and Co_3O_4 could be observed when further discharged, indicating their consumption during the discharge process. However, no diffraction peaks related to discharge products showed up, arising from their low crystallinity or amorphous states. This phenomenon has been reported in previous literature.[6] At a fully charged state, the diffraction peaks of ZnO and Co_3O_4 reappeared, demonstrating their reversible generation.

18

The rate performance was examined at different current densities (**Fig. 6b**). ZnO/Co_3O_4 showed the most fascinating capacity retention ability compared with single components and their physical mix. The charge/discharge profiles were exhibited in **Fig. S20**. As shown, ZnO/Co_3O_4 retained the voltage plateau well at all current densities. The excellent lithium storage performance of as-prepared walnut-like ZnO/Co_3O_4 porous nanospheres was superior to most reported ZnO, Co_3O_4 and ZnO/Co_3O_4 composites for LIBs (**Fig. S21**).

The superior lithium storage performance of walnut-like ZnO/Co_3O_4 arises from several aspects: (1) the nanometer size enhances the reaction kinetics due to facilitated electron/ion transport, and eases the mechanical strain caused by volume variation. (2) the large specific surface area provides abundant reactive sites, which is more beneficial with capacitive behavior, enhancing lithium storage and migration. (3) the rational hybridization of ZnO and Co_3O_4 endows the composite with high conductivity and structural stability, guaranteeing long-term cycling durability. (4) the abundant channels provided by the walnut-like structure facilitate ion/electron diffusion, thus ensuring fast charge transfer. (5) the space alleviates huge volume variation throughout the cycling process, achieving excellent structural integrity and cycling durability.
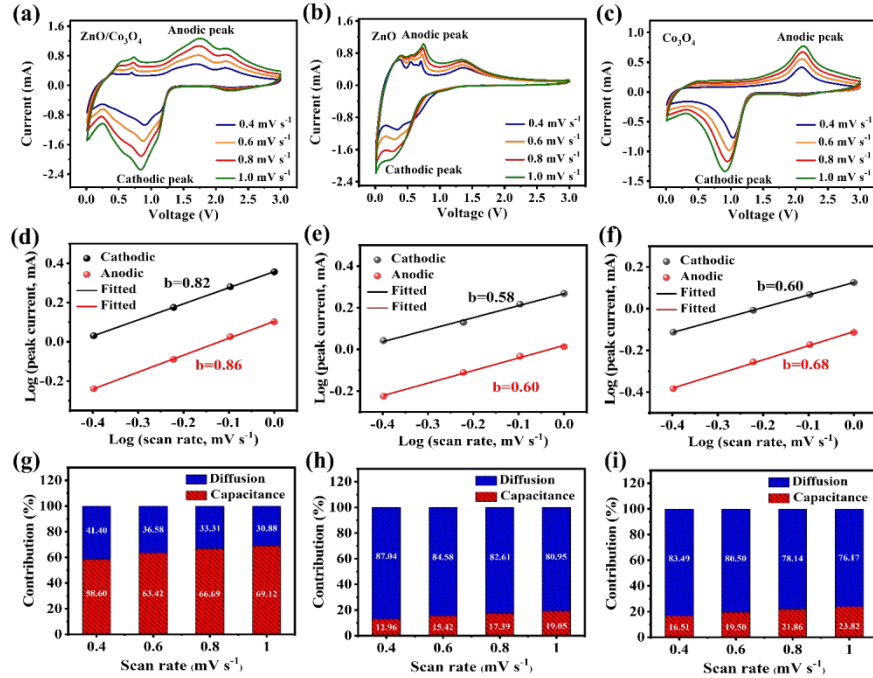
Fig. 7 CV curves of (a) ZnO/Co$_3$O$_4$, (b) ZnO and (c) Co$_3$O$_4$ at scan rates of 0.4, 0.6, 0.8 and 1.0

mV s^{-1}. Corresponding log *i versus* log *v* of (d) ZnO/Co$_3$O$_4$, (e) ZnO and (f) Co$_3$O$_4$.

Diffusion/capacitance contribution ratio for (g) ZnO/Co$_3$O$_4$, (h) ZnO and (i) Co$_3$O$_4$.

To further understand kinetics characteristics of ZnO/Co$_3$O$_4$, ZnO and Co$_3$O$_4$ towards lithium

storage, CV curves were collected at scan rates of 0.4, 0.6, 0.8 and 1.0 mV s^{-1} (**Fig. 7a-7c**). In

general, the current intensity increases as the scanning rate raises. The charge storage kinetics were

evaluated by b from the equation below:[41]

$$i = av^b \qquad (2)$$

For a capacitor-type electrode, the b value is 1.0, and for a battery-type electrode, the b value

approaches 0.5. As revealed in **Fig. 7d**, the b values calculated based on Eq. (1) were 0.82 and

0.86 for cathodic and anodic peaks, respectively, suggesting a capacitive dominant charge storage

mechanism. As expected, the larger b value of ZnO/Co_3O_4 confirms that the 3D porous walnut-like structure was more favorable to Li^+ storage occurring near the surface.

$$i(v) = k_1v + k_2v^{1/2} \qquad\qquad (3)$$

Furthermore, the diffusion/capacitation contribution ratio can be quantitatively investigated according to Eq. (3).[44] **Fig. S22** reveals k_1 and k_2 values from $i(v)/v^{1/2}$ versus $v^{1/2}$ plot. As shown in **Fig. 7**, the capacitation contributions of ZnO/Co_3O_4 were 58.60, 63.42, 66.69 and 69.12 at different scan rates. The kinetics analysis demonstrated that diffusion-controlled and capacitive behaviors occurred simultaneously in ZnO/Co_3O_4. The capacitive process involves surface redox reactions, which are related to rapid electron diffusion, fast mass transport, and large accessible active sites. The amazing pseudocapacitive behavior of ZnO/Co_3O_4 arises from its unique walnut-like porous nanostructure, favorable conductive pathways, and large surface area, which is conducive to exert superior lithium storage performance.

4. Conclusions

In summary, this work developed an in-situ fabrication of hybridized ZnO/Co_3O_4 porous nanospheres (ca. 200 nm in size) with mesoporous ravines on the surface. Such advantageous nanoarchitecture can provide several excellent properties: abundant pores to shorten the distance for Li^+ diffusion, ultrafine ravines to accommodate the volume change and large surface area to facilitate surface redox reactions. Besides, the in-situ fabrication of ZnO and Co_3O_4 brought a synergistic effect, and $ZnO-Co_3O_4$ heterostructure promoted redox kinetics and enhanced

structural stability. Thus, assembled anode based on rationally designed walnut-like ZnO/Co_3O_4 composite exhibited high reversible capacity, excellent rate capability and impressive long-term cyclability. We believe that the bi-component ZnO/Co_3O_4 with walnut-like architecture is promising as a commercial electrode material for LIBs, and the facile strategy can be extended to design new TMO-based materials for energy storage applications.

Conflicts of interest

The authors declare no conflicts.

Acknowledgements

References

1   D. Wang, H. Liu, Z. Shan, D. Xia, R. Na, H. Liu, B. Wang and J. Tian, *Energy Storage Mater.*, 2020, **27**, 387–395.

2   I. Yoon, S. Jurng, D. P. Abraham, B. L. Lucht and P. R. Guduru, *Energy Storage Mater.*, 2020, **25**, 296–304.

3   Y. Zhang, Y. Zhang, A. Mathur, S. Ben-Yoseph, S. Xia, Y. Wu and N. Liu, *J. Power Sources*, 2021, **491**, 229547.

4   Y. Zhao, G. Huang, Y. Li, R. Edy, P. Gao, H. Tang, Z. Bao and Y. Mei, *J. Mater. Chem. A*, 2018, **6**, 7227–7235.

5   X. Lv, W. Wei, B. Huang and Y. Dai, *J. Mater. Chem. A*, 2019, **7**, 2165–2171.

6   J. Li, D. Yan, S. Hou, T. Lu, Y. Yao, D. H. C. Chua and L. Pan, *Chem. Eng. J.*, 2018, **335**, 579–589.

7   X. Tang, M. Liang, Y. Zhang, W. Sun and Y. Wang, *Dalt. Trans.*, 2019, **48**, 4413–4419.

8   Y. T. Liu, P. Zhang, N. Sun, B. Anasori, Q. Z. Zhu, H. Liu, Y. Gogotsi and B. Xu, *Adv. Mater.*, 2018, **30**, 1–9.

9   L. Lu, H. Wang, J.-G. Wang, C. Wang and Q. Jiang, *J. Mater. Chem. A*, 2017, **5**, 2530–2538.

10   Y. Zhao, X. Li, B. Yan, D. Xiong, D. Li, S. Lawes and X. L. Sun, *Adv. Energy Mater.*, 2016, **6**, 1502175.

11   J. Zheng, C. He, X. Li, K. Wang, T. Wang, R. Zhang, B. Tang and Y. Rui, *J. Alloys Compd.*, 2021, **854**, 157315.

12   W. An, B. Gao, S. Mei, B. Xiang, J. Fu, L. Wang, Q. Zhang, P. K. Chu and K. Huo, *Nat. Commun.*, 2019, **10**, 1–11.

13   X. Ge, Z. Li, C. Wang and L. Yin, *ACS Appl. Mater. Interfaces*, 2015, **7**, 26633–26642.

14   Z. Wang, H. Duan, X. Meng, Y. Zhang and H. Qi, *Macromol. Res.*, 2016, 24, 757-766.

15   R. Cha, J. Li, Y. Liu, Y. Zhang, Q. Xie and M. Zhang, *Colloids Surfaces B Biointerfaces*, 2017, 158, 213-221.

16   F. Lyu, S. Zeng, Z. Sun, N. Qin, L. Cao, Z. Wang, Z. Jia, S. Wu, F. X. Ma, M. Li, W. Wang, Y. Y. Li, J. Lu and Z. Lu, *Small*, 2019, **15**, 1–9.

17   M. Yu, X. Bian, S. Liu, C. Yuan, Y. Yang, X. Ge, R. Guan and C. Wang, *ACS Appl. Mater.*

Interfaces, 2019, **11**, 25254–25263.

18   H. Sancho, Y. Y. Zhang, L. Liu, V. G. Barevadia, S. Wu, Y. Y. Zhang, P.-W. Huang, Y. Y. Zhang, T.-H. Wu, W. You and N. Liu, *J. Electrochem. Soc.*, 2020, **167**, 056503.

19   Y. Zhang, Y. Wu, W. You, M. Tian, P. W. Huang, Y. Zhang, Z. Sun, Y. Ma, T. Hao and N. Liu, *Nano Lett.*, 2020, **20**, 4700–4707.

20   Y. Zhang and N. Liu, *Chem. Mater.*, 2017, **29**, 9589–9604.

21   Y. Zhang, Y. Wu, H. Ding, Y. Yan, Z. Zhou, Y. Ding and N. Liu, *Nano Energy*, 2018, **53**, 666–674.

22   C. Li, C. Zhang, J. Xie, K. Wang, J. Li and Q. Zhang, *Chem. Eng. J.*, 2021, **404**, 126463.

23   Y. Zhang, Y. Zhang, Y. Cao, M. Xie, J. Li, A. Balzer, N. Liu and Z. John Zhang, *Chem. – A Eur. J.*, 2021, 27, 12900-12909.

24   L. Wang, X. Cui, L. Gong, Z. Lyu, Y. Zhou, W. Dong, J. Liu, M. Lai, F. Huo, W. Huang, M. Lin and W. Chen, *Nanoscale*, 2017, **9**, 3898–3904.

25   W. Li, Z. Gong, X. Yan, D. Wang, J. Liu, X. Guo, Z. Zhang and G. Li, *J. Mater. Chem. A*, 2019, **8**, 433–442.

26   Y. Zhang, M. Xie, Y. He, Y. Zhang, L. Liu, T. Hao, Y. Ma, Y. Shi, Z. Sun, N. Liu and Z. John Zhang, *Chem. Eng. J.*, 2021, **420**, 130469.

27   S. Hao, B. Zhang, J. Feng, Y. Liu, S. Ball, J. Pan, M. Srinivasan and Y. Huang, *J. Mater. Chem. A*, 2017, **5**, 8510–8518.

28   C. He, B. Han, S. Han, Q. Xu, Z. Liang, J. Y. Xu, M. Ye, X. Liu and J. Xu, *J. Mater. Chem. A*, 2019, **7**, 26884–26892.

29   S. Grugeon, S. Laruelle, L. Dupont and J.-M. Tarascon, *Solid State Sci.*, 2003, **5**, 895–904.

30   Y. Zhang, Q. Zhuo, X. Lv, Y. Ma, J. Zhong and X. Sun, *Electrochim. Acta*, 2015, **178**, 590–596.

31   D. Lin, Z. Lu, P. C. Hsu, H. R. Lee, N. Liu, J. Zhao, H. Wang, C. Liu and Y. Cui, *Energy Environ. Sci.*, 2015, **8**, 2371–2376.

32   H. Lv, Y. Guo, Z. Yang, Y. Cheng, L. P. Wang, B. Zhang, Y. Zhao, Z. J. Xu and G. Ji, *J. Mater. Chem. C*, 2017, **5**, 491–512.

33   J. Li, D. Yan, S. Hou, T. Lu, Y. Yao and L. Pan, *Chem. Eng. J.*, 2018, **354**, 172–181.

34   M. Liu, H. Fan, O. Zhuo, J. Chen, Q. Wu, L. Yang, L. Peng, X. Wang, R. Che and Z. Hu,

Nano Energy, 2020, **68**, 104368.

35   H. Chen, L. Deng, S. Luo, X. Ren, Y. Li, L. Sun, P. Zhang, G. Chen and Y. Gao, *J. Electrochem. Soc.*, 2018, **165**, A3932–A3942.

36   J. Bai, K. Wang, J. Feng and S. Xiong, *ACS Appl. Mater. Interfaces*, 2015, **7**, 22848–22857.

37   F. Zou, Y. M. Chen, K. Liu, Z. Yu, W. Liang, S. M. Bhaway, M. Gao and Y. Zhu, *ACS Nano*, 2016, **10**, 377–386.

38   L. Yang, H.-S. Chen, W.-L. Song and D. Fang, *ACS Appl. Mater. Interfaces*, 2018, **10**, 43623–43630.

39   J. Guo, Q. Liu, C. Wang and M. R. Zachariah, *Adv. Funct. Mater.*, 2012, **22**, 803–811.

40   H. Hu, J. Zhang, B. Guan and X. W. D. Lou, *Angew. Chemie - Int. Ed.*, 2016, **55**, 9514–9518.

41   J. Li, J. Li, T. Chen, T. Lu, W. Mai and L. Pan, *Inorg. Chem. Front.*, 2019, **6**, 694–704.

42   B. Chen, H. Qin, K. Li, B. Zhang, E. Liu, N. Zhao, C. Shi and C. He, *Nano Energy*, 2019, **66**, 104133.

43   J. Li, D. Yan, T. Lu, Y. Yao and L. Pan, *Chem. Eng. J.*, 2017, **325**, 14–24.

44   F. Niu, J. Yang, N. Wang, D. Zhang, W. Fan, J. Yang and Y. Qian, *Adv. Funct. Mater.*, 2017, **27**, 1–11.